Self-Calibration of the Breaker Index from Fixed-Camera Wave Heights

Ketron Mitchell-Wynne[1], Michael Reinwald[1], Francisco Sansana Silva[1], Daniel Thompson[1], Zane D'Amico[1], Mercedes Stringer[1], Benjamin Freeston[1]

[1]Surfline Coastal Intelligence, Surfline/Wavetrak, Inc., San Francisco, California 94114, U.S.A.

This manuscript is a **non-peer reviewed preprint** submitted to EarthArXiv. This manuscript has been submitted to *Coastal Engineering* for peer review. Subsequent versions may differ in content; if accepted for publication, the peer-reviewed version will be linked from this preprint's EarthArXiv landing page. Please feel free to contact the corresponding author with any feedback.

Corresponding author Ketron Mitchell-Wynne <kwynne@surfline.com>

ORCID (submitter) https://orcid.org/0009-0007-4269-4804

License Creative Commons Attribution–NonCommercial 4.0 International (CC BY-NC 4.0)

Peer-review status Submitted to *Coastal Engineering* (Elsevier), under review

Keywords bathymetry; wave tracking; coastal cameras; breaker index; self-calibration; tide; depth inversion

Self-Calibration of the Breaker Index from Fixed-Camera Wave Heights

Ketron Mitchell-Wynne[a,*], Michael Reinwald[a], Francisco Sansana Silva[a], Daniel Thompson[a], Zane D'Amico[a], Mercedes Stringer[a], Benjamin Freeston[a]

[a]*Surfline Coastal Intelligence, Surfline/Wavetrak, Inc., San Francisco, 94114, California, U.S.A.*

Abstract

Depth inversions from breaking waves usually assume a breaker index γ, the ratio of breaking height to water depth. Where breaking is depth-limited, the height at a fixed location rises and falls with the tide at the rate γ. Breaking waves tracked in video from fixed coastal cameras therefore can give the index from this tide response and the depth from the mean breaking height, with no survey, beach slope or wave model. This method is tested on eleven cameras around Oceanside, California, against two bathymetric surveys a season apart, using 14 days of video before each survey. The RMSE is 0.36 m on three cameras in Fall and 0.47 m on ten in January. The spatial validation shows a better agreement and reaches shallower depths than the satellite derived bathymetry using Sentinel-2. At Tamarack Beach, a beach break, the self-calibrated breaker index is 0.50 in Fall and 0.59 in January. With these indices the recovered mean depth agrees with both surveys to within 0.1 m, and cell by cell the RMSE is 0.32 and 0.42 m.

Keywords: bathymetry, wave tracking, coastal cameras, breaker index, self-calibration, tide, depth inversion

1. Introduction

Where waves break, how sand moves along the coast, and how far storm waves run up a beach are all influenced by the nearshore bathymetry. Relative to traditional observation methods, surf zone bathymetry can change quickly and is difficult to observe. Survey boats with single-beam, multibeam or side-scan sonar are slow and expensive, and they cannot work safely in less than about a meter of water. That leaves a gap between the low-tide line and the shallowest boat track. Airborne lidar is also expensive and infrequent, and foam and turbid water degrade it, as they degrade satellite imagery. Walking or wading RTK surveys reach only a narrow band near low tide. None of these methods keeps pace with the seabed changes, so the surf zone is the least current part of most nearshore maps (Ruessink et al., 2009; Plant et al., 1999). Surveys are scarce beyond the surf zone as well: close to half of the world's coastal waters remain unsurveyed (Cesbron et al., 2021).

Most depth inversions from shore-based cameras estimate depth from wave celerity, the speed at which wave crests travel (Holman and Haller, 2013). Stockdon and Holman (2000) estimate the cross-shore wavenumber from pixel-intensity time series and invert the linear dispersion relation for depth. Holman et al. (2013) extends this to two dimensions as cBathy, now the standard algorithm for fixed-camera networks. Against 39 surveys at Duck, NC, its current version has a bias of 0.08 m, an RMSE of 0.38 m and a 95% exceedance of 0.78 m (Holman and Bergsma, 2021). On commercial streaming webcams, Andriolo et al. (2025) report a mean bias of 0.05 m and a mean RMSE of 0.43 m over depths down to 10 m. That range includes water seaward of the surf zone. With a non-linear phase-speed relation for breaking waves, Catalán and Haller (2008) reduced the relative depth error on a laboratory median profile from 32% RMS with linear theory to 10% RMS, where the percentage is the depth error divided by the true depth. The 0.38 m and 0.43 m above are absolute errors from field surveys.

Breaking degrades these inversions in two ways. A breaking crest travels faster than linear theory predicts, so the inverted depth is too large (Stockdon and Holman, 2000; Bergsma and Almar, 2018). The tracked brightness feature also moves from the dark wave front to the white foam, which Bergsma et al. (2019) show adds a large depth overestimate at the breakpoint. Brodie et al. (2018) find the surf-zone bar crest displaced tens of meters shoreward once the offshore wave height exceeds about 1.2 m, and the recommended practice for cBathy is to discard such collections (Holman and Bergsma, 2021). Lange et al. (2023) track individual crests with a neural network inside the surf zone and join the result to cBathy offshore. From a hovering drone they reach a surf-zone RMSE of 0.17 m.

The tide has been used as a known vertical reference for the intertidal beach. Mapping the imaged waterline against the measured water level over the tidal cycle gives the intertidal profile (Holman et al., 1991; Plant and Holman, 1997). Aarninkhof et al. (2003) corrected the waterline elevation for runup and setup. Uunk et al. (2010) and Soloy et al. (2021) automated the method for continuous

*Corresponding author.
Email address: kwynne@surfline.com (Ketron Mitchell-Wynne)

operation, with vertical errors of 0.18–0.34 m (Uunk et al., 2010; Vousdoukas et al., 2011). A waterline gives the elevation of ground that the tide uncovers, so the map ends at the low-tide line, covers only the observed tidal range (about 1.4 m at Egmond and 1 m at Duck) and loses accuracy on steeper beaches (Salameh et al., 2019).

Celerity inversions are degraded where waves break, and a waterline map ends at the low-tide line. Depth below that line has been inferred from the breaking itself. Aarninkhof and Ruessink (2004) showed that time-averaged image brightness can be read as the dissipation of breaking waves. Aarninkhof et al. (2005) inverted that signal over a year of hourly images at Egmond and obtained a profile-averaged RMS difference of about 0.4 m. The same signal drives the assimilation schemes of van Dongeren et al. (2008), Birrien et al. (2013) and Wilson et al. (2014). All of these schemes run a wave model forced at the offshore boundary, because dissipation is informative only against such a model. Aarninkhof et al. (2005) needed a heuristic scaling function near the shoreline.

Optical satellite-derived bathymetry (SDB) retrieves depth from the log-ratio of two visible bands, which is close to linear in depth once calibrated on known depths (Stumpf et al., 2003). Sentinel-2 images the world's coasts at 10 m resolution about every 5 days, and the imagery is open (Drusch et al., 2012). In clear water, Caballero and Stumpf (2019) report median absolute errors of 0.22–0.5 m over 0–18 m depth in South Florida from five to ten calibration depths. Frugier et al. (2026) invert a decade of Sentinel-2 and VENμS imagery at Duck. The color signal fails inside the breaking zone, so they calibrate on breaking positions detected in the images, with the ratio of breaking height to local depth set to 0.36.

The depth-limited breaking relation

$$H = \gamma\, h \tag{1}$$

links the height H of a breaking wave to the local still-water depth h through the breaker index $\gamma = H/h$. It holds where a wave breaks because the water is too shallow for its height; such locations are called saturated. Seaward of the breakpoint the wave is still shoaling, $H < \gamma h$, and a saturated inversion applied there makes the water too shallow.

Published values of γ span roughly 0.3 to 1.2. They differ because they use different heights, different summaries over many waves and different breaker types (McCowan, 1894; Miche, 1944; Weggel, 1972; Sallenger and Holman, 1985; Camenen and Larson, 2007; Goda, 1970, 2010; Battjes and Janssen, 1978; Battjes and Stive, 1985; Zhang et al., 2021). Since $h = H/\gamma$, the index scales the recovered depth directly. Even for one wave statistic the published range is wide: the Sallenger–Holman values 0.29–0.55 differ by nearly a factor of two in depth. Operational inversions usually impose one literature value (Salmon et al., 2015; Holthuijsen, 2007), and the steepness-dependent forms need the offshore steepness from a wave model. Sec. 2.2.7 gives the wave height each of these values refers to.

Surfline's fixed coastal cameras provide georeferenced video from which the face heights of individually tracked breaking waves are measured (Reinwald et al., 2026). At a fixed location the seabed is taken as steady while the tide dithers - raises and lowers the water by a known amount. Under saturated breaking, the breaker height therefore rises and lowers with the tide at a rate equal to γ, and the mean wave height across the tide gives the depth. This slope is fitted at fixed locations across the surf zone (Fig. 1), and the index is read where the fitted slopes are largest, in the cross-shore band of saturated breaking; the value read this way is called the self-calibrated breaker index. No beach slope, offshore spectrum, wave model or survey is required for the inversion. The idea comes from observational astronomy, where telescope pointing is dithered so that different detector pixels see the same fixed celestial positions, and the unknown gain and offset of every pixel are solved together with the constant sky brightness at each position (Fixsen et al., 2000). Telescopic dithering is analogous to tidal dithering in this work, and the sky brightness at fixed celestial positions to the water depth at fixed points on the seabed. For this the imaged surf zone is divided into a grid of square cells a few meters on a side, fixed in geographic coordinates so that they do not move with the camera's pan, tilt or zoom, and every tracked wave height is assigned to the cell in which it was measured. Wave face heights are measured in each daylight clip, and from them the method maps depth in the band between the low-tide line and the deepest saturated cells.

The inversion is tested on eleven cameras around Oceanside, California, against two bathymetric surveys a season apart. One of them, Tamarack Beach in Carlsbad, has the largest overlap with the surveys and is analyzed in the most detail. There the self-calibrated index, obtained without the survey, is checked against the level-matching index: the value of γ that would make the recovered mean depth equal the surveyed mean depth. Over all eleven cameras the inversion is then compared with fixed literature indices and with Sentinel-2 SDB.

2. Data and methods

2.1. Data

2.1.1. Camera wave heights

Surfline's processing pipeline segments commercial pan-tilt-zoom video at 1 Hz, tracks individual breaking waves and measures their wave face height (Reinwald et al., 2026). The segmentation separates the wave face, the pocket (the steep part of the face just ahead of the breaking crest) and whitewater. A wave track follows one breaking wave from formation to dissipation and records its face height at known world locations. Video is processed in 10-minute clips. Each clip is georeferenced with its own tide, time and pan-tilt-zoom setting (Reinwald et al., 2026), and the tide is taken as constant within each 10-minute interval.

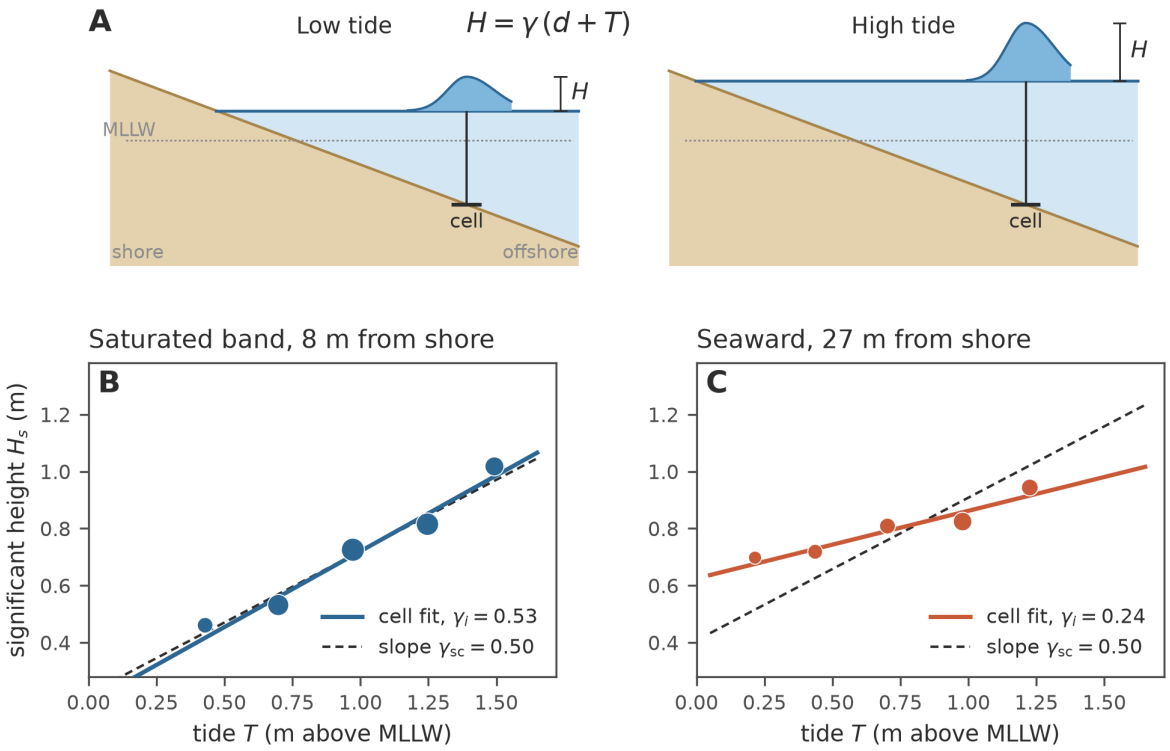


Figure 1: Tide response of breaking height at Tamarack in the Fall-2025 window. **(A)** Schematic cross-section of one cell at low tide and at high tide, not to scale. The still-water depth is the seabed depth d below MLLW plus the tide T. Where breaking is saturated, $H = \gamma(d + T)$, so the breaking height rises with the tide. **(B)** Significant wave height against tide for an example cell 8 m from shore, in the band the index is read from (Sec. 2.2.5). The solid line is the weighted fit in that cell; the dashed line has slope $\gamma_{sc} = 0.50$. Marker area is the number of waves in the tide bin. **(C)** An example cell 27 m from shore, seaward of that band. Both cells are taken from the index table (Sec. 2.2.1). The figure shows the tide slope the index is read from, in the saturated band and seaward of it.

2.1.2. Grid cells and projection range

The imaged surf zone is divided into a grid of square cells fixed in geographic coordinates. Each breaking-wave height is assigned to the cell containing its pocket position, so the same cell receives heights from every clip and pan-tilt-zoom setting that views it. Pocket positions come from the camera's pixel-to-ground homography, the mapping between the still-water plane and the image (Reinwald et al., 2026). The still-water plane moves with the tide, so each clip is projected at its own tide (Sec. 2.1.1). The projected position remains uncertain, and that uncertainty grows with range from the camera. The cell size is set from it: on the grids used for the depth inversion the cell edge is the 90th percentile, over the surf zone, of the 1σ position error along its major axis, limited to 3–6 m. The per-cell slope maps of Sec. 3.1 use finer cells of 2–4 m. Because cell sizes differ between grids, cell counts are quoted with the area they cover.

2.1.3. Tide and offshore waves

The tide T of each clip is the harmonic prediction of Surfline's tide service for the station assigned to the camera's surf spot, interpolated to the clip time. The service runs XTide (Flater, 2026) on the NOAA subordinate station San Clemente, California (XTide TWC0419), whose predictions are a reference station's harmonic constants with fixed time and height offsets, referenced to mean lower low water (MLLW). All eleven cameras are assigned this station. Offshore wave conditions come from LOTUS, Surfline's spectral wave model based on WAVEWATCH III (Surfline, 2020). Wave data are extracted from its regional nearshore grids at 3' resolution.

At the grid point assigned to each spot, LOTUS provides the hourly directional wave spectrum. From it we extract the significant wave height, $H_s = 4\sqrt{m_0}$, where m_0 is the zeroth moment of the spectrum, the peak period, T_p, at the spectral maximum, and the deep-water steepness, $s_0 = H_{\mathrm{rms},\infty}/L_0$, with $H_{\mathrm{rms},\infty} = H_s/\sqrt{2}$ and $L_0 = gT_p^2/2\pi$. Each is reduced to a daily median. These offshore values are used only to check the swell–tide coupling and to set the Battjes–Stive fixed index. They are not required for the inversion.

2.1.4. Study sites

The eleven cameras of the study view about 8 km of coast from Oceanside Harbor south to Tamarack Beach

in Carlsbad, California, largely within the two surveys (Fig. 2A). From north to south they are three views of Oceanside Harbor and its jetties, two of Oceanside Pier, Tyson Street, two of artificial surf reefs, The Rock, North Carlsbad and Tamarack. Tamarack is a gently sloping sand beach break with spilling breakers and is analyzed in the most detail. A plane fitted to the survey depths over its scored cells gives a surf-zone slope $\tan\beta$ of about 1:60 in Fall and 1:50 in January.

2.1.5. Bathymetric surveys

The RE:BEACH monitoring program of the City of Oceanside (GHD, 2026) surveyed the Oceanside coast twice. The Fall-2025 campaign combined a wide vessel survey with two detailed nearshore patches at Oceanside Pier, and the January-2026 campaign made a wide survey of the same coast. Both wide surveys are delivered as depth grids of 5 m cells. The two patches are 1.5 m grids interpolated from the contours of a merged survey and lidar product, and they are used only inside the area those contours cover. The wide surveys cover 7.1 and 7.4 km of coast at similar median depth (9.3 and 9.0 m) and are separated by one winter. Survey elevations are converted to depth in meters below MLLW. Three cameras are scored against the Fall survey and ten of the eleven against the January survey (Sec. 2.3).

2.2. Self-calibration of the breaker index

2.2.1. Wave statistics and height tables

Two choices define the height assigned to each cell and tide bin: the height retained from each tracked wave and the statistic taken over all waves in the bin. The per-wave height is the mean along the track (mean), the mean of its three largest heights (top3mean) or its largest height (max). The last two depend on the 1 Hz sampling of the track (Sec. 2.1.1): the three largest heights in a track are three 1-second samples, so top3mean averages the face height over about three seconds around the moment the track's height is greatest, and a different frame rate would give a different height. The cell statistic is the mean, root-mean-square, significant wave height H_s (the mean of the largest third), $H_{1/10}$, a percentile or the maximum. The pair is written (per-wave height, cell statistic). Values more than three standard deviations from the cell-and-tide-bin mean are discarded before the cell statistic is computed.

Two height tables are built from the same clips, and both use H_s as the cell statistic. The index table uses (top3mean, H_s): it keeps one top3mean height per wave, placed at the cell of its tallest pocket, so that each wave enters it once, where it is tallest. The depth table uses (max, H_s): it keeps the largest pocket height in every cell that a wave crosses from its tallest pocket shoreward, so that every cell the broken wave passes over receives a height. A cell and tide bin enters a table only if at least ten waves contribute, and a cell holds data if at least one of its tide bins does. The index table is used only to estimate the index, and the depth table is converted to depth with that index held fixed. Two tables are needed because the tide slope requires each height to be tied to the cell where it is realized, whereas the depth requires a height in every cell a wave crosses. The tables share the cell statistic and differ in the waves that populate each cell, and in the saturated band the heights of both populations are set by the local depth. Whether the index transfers between the tables is tested at Tamarack by the level-matching index of Sec. 3.2. At Tamarack in the Fall window the index table holds data in 574 cells and the depth table in 1,550 cells.

2.2.2. Forward model at a fixed cell

The grid cells of Sec. 2.1.2 are indexed by i. The still-water depth at cell i is

$$h_i(t) = d_i + T(t), \tag{2}$$

where d_i is the unknown, time-invariant seafloor depth below MLLW and $T(t)$ is the tide elevation above that datum at time t. Where the wave is depth-limited, substituting (2) into (1) with additive measurement noise ε gives the forward model at a fixed cell,

$$H_i(t) \;=\; \gamma\,\big(d_i + T(t)\big) + \varepsilon. \tag{3}$$

The depth d_i enters (3) only through the per-cell intercept $a_i \equiv \gamma\, d_i$, which is constant in time, so the model has one parameter γ common to all cells and one intercept per cell.

2.2.3. Tide response and swell–tide coupling

Self-calibration here means reading γ from the tide response and the depth from the mean wave height, both from the same data. Within an analysis window (Sec. 2.2.9) both the tide $T(t)$ and the offshore steepness $s_0(t)$ vary, and several parameterizations make the index a function of steepness, $\gamma = \gamma(s_0)$ (Battjes and Stive, 1985; Zhang et al., 2021). Writing $\gamma'(s_0) \equiv d\gamma/ds_0$ and treating the seafloor depth d_i as constant, the forward model (3) and its tide derivative at fixed d_i are

$$H_i(t) = \gamma\big(s_0(t)\big)\, d_i + \gamma\big(s_0(t)\big)\, T(t) + \varepsilon, \tag{4}$$

$$\left.\frac{\partial H_i}{\partial T}\right|_{d_i} = d_i\,\gamma'(s_0)\left.\frac{\partial s_0}{\partial T}\right|^{\text{fit}} + \gamma(s_0) + T\,\gamma'(s_0)\left.\frac{\partial s_0}{\partial T}\right|^{\text{fit}} \tag{5}$$

$$= \gamma(s_0) + \underbrace{(d_i + T)\,\gamma'(s_0)\left.\frac{\partial s_0}{\partial T}\right|^{\text{fit}}}_{\text{swell–tide coupling}}, \tag{6}$$

where $\partial s_0/\partial T|^{\text{fit}}$ is the within-window covariation of steepness with tide, not a physical dependence. Where the swell is steady or uncorrelated with the tide this term vanishes, and

$$\left.\frac{\partial H_i}{\partial T}\right|_{d_i,\,s_0} \;=\; \gamma, \tag{7}$$

so neither the depth nor the intercept appears. The slope is the breaker index of the wave statistic that forms the



Figure 2: Survey footprints, camera fields and recovered depth. **(A)** Location map of the eleven cameras around Oceanside over satellite imagery, with the simplified footprints of the Fall-2025 survey (dashed amber) and the January-2026 survey (solid teal), which share their offshore edge, each camera's field outline and name, a north arrow and a 1000 m scale bar. White boxes mark the zoom panels. **(B–I)** January-2026 zooms on four camera clusters, from north to south Oceanside Harbor (B, C), Oceanside Pier to the artificial reefs (D, E), The Rock (F, G) and North Carlsbad and Tamarack (H, I), each with a north arrow and scale bar. The left panel of each pair shows the depth recovered on the 14-day window before the survey, with each camera's mean offset to the survey removed, and the right panel the survey depth over the same area, on one scale from 0 to 5 m below MLLW. The offsets are listed in Table 1; for Artificial Reef 1 it is taken from its 49 overlapping cells. White outlines trace each camera's field and dashed inner outlines the cells scored against the survey. The Fall-2025 results are in Table 1 and Fig. 4. Imagery © Esri. The figure places the cameras on the two surveys and lets the spatial pattern of each recovered field be compared with the survey beneath it.

cell heights (Sec. 2.2.1). The seabed does change over two weeks, so this is an approximation: a change in d_i that is correlated with the tide remains in the fitted slope. The windows are kept to 14 days (Sec. 2.2.9).

When s_0 does covary with the tide inside the window, the coupling term in (6) remains in the fitted slope. Writing $\rho_{Ts_0} \equiv \mathrm{corr}(T, s_0)$, so that $\partial s_0/\partial T|^{\mathrm{fit}} = \rho_{Ts_0}\,\sigma_{s_0}/\sigma_T$, and linearizing about the window mean $\langle s_0\rangle$ with $h_i = d_i + T$, the slope at cell i is biased by

$$\mathrm{Bias}\big[\hat{\gamma}\big]_i \;\approx\; \langle h_i\rangle\,\gamma'\big(\langle s_0\rangle\big)\,\rho_{Ts_0}\,\sigma_{s_0}/\sigma_T. \tag{8}$$

The bias is small in a short window with steady swell, where $\sigma_{s_0}/\langle s_0\rangle \ll 1$, and it grows where the tidal range σ_T is small, so the analysis windows of Sec. 2.2.9 require a minimum tide span. Tide and swell are physically independent, but finite and daylight-only sampling can correlate them within a window. Sec. 3.6 measures that correlation.

2.2.4. Common-slope fit and depth inversion

For either height table, $H_{i,b}$ is the cell statistic in cell i and tide bin b, and the number of contributing waves gives its weight $W_{i,b}$. The tide response is evaluated as a difference between tide bins $b = 0, \ldots, B-1$ of the same cell. With count-weighted cell means

$$\bar{H}_i = \frac{\sum_b W_{i,b}\,H_{i,b}}{\sum_b W_{i,b}}, \qquad \bar{T}_i = \frac{\sum_b W_{i,b}\,T_{i,b}}{\sum_b W_{i,b}}, \tag{9}$$

subtracting each cell's mean removes its unknown intercept,

$$H_{i,b} - \bar{H}_i = \gamma\left(T_{i,b} - \bar{T}_i\right) + \varepsilon, \tag{10}$$

and weighted least squares gives one slope shared by all cells, the common slope $\hat{\gamma}$,

$$\hat{\gamma} = \frac{\sum_{i,b} W_{i,b}\,(T_{i,b} - \bar{T}_i)(H_{i,b} - \bar{H}_i)}{\sum_{i,b} W_{i,b}\,(T_{i,b} - \bar{T}_i)^2}. \tag{11}$$

The fit has cell fixed effects: each cell keeps its own free intercept, and the slope is common. The denominator of (11) is the tide variance within each cell, so a cell seen at a single tide level adds nothing, and the tidal range limits how well the slope is determined. Arendt et al. (2000) discuss the same constraint for detector calibration in observational astronomy. The cell means then give each depth,

$$\hat{d}_i = \frac{a_i}{\hat{\gamma}} = \frac{\bar{H}_i}{\hat{\gamma}} - \bar{T}_i. \tag{12}$$

2.2.5. Self-calibrated index

Fitting (10) in each cell separately gives the per-cell tide slope γ_i. Cells where waves are not depth-limited ($H < \gamma h$) return slopes below γ. They include cells seaward of the break, where waves are still shoaling, cells where waves decay after breaking farther out, and the swash zone. Against distance from shore, γ_i therefore rises to a plateau in the band of saturated breaking, and the index is read there. The distance from shore of a cell is the mean, over the waves whose tallest pocket lies in it, of that pocket's distance to the shoreline detected in the same clip. The index-table cells with a positive slope are grouped by this distance into ten bins with equal numbers of cells. The self-calibrated index γ_{sc} is the median γ_i over the bin with the largest median γ_i and its two neighbors. Reading the index from the plateau excludes the cells that are not depth-limited. The common slope $\hat{\gamma}$ of (11), by contrast, is fitted over every cell of the index table, so those cells enter it and pull it down; it is reported only for comparison (Sec. 3.1), and the depth fields of this paper use γ_{sc} in place of $\hat{\gamma}$ in (12). The depth field itself keeps every cell, whatever its slope, because the depth comes from the cell mean and not from the per-cell slope. A separate index and depth field are estimated from each camera's heights, tide record and grid, using the analysis windows of Sec. 2.2.9.

2.2.6. Height errors

A constant error in H, or a datum offset between the tide record and the survey, enters (3) only through the intercept $a_i = \gamma d_i$. It cancels when each cell's mean is removed, so $\hat{\gamma}$ and the γ_i are unaffected, but it shifts the depth field vertically.

2.2.7. Relation to published breaker indices

The McCowan limit $\gamma \approx 0.78$ is the height-to-depth ratio at which a solitary wave on a flat bottom just becomes vertical (McCowan, 1894). The Goda plunging value 0.83 is the tabulated breakpoint of a regular wave on a moderate slope (Goda, 1970, 2010). Battjes and Janssen (1978) modeled breaking in a random sea by capping the wave-height distribution at a maximum height $H_m = \gamma h$, with $\gamma = 0.8$. Battjes and Stive (1985) calibrated that γ against laboratory and field data and made it depend on offshore steepness, $\gamma = 0.5 + 0.4\tanh(33 s_0)$. Averaged over all waves the ratio is lower: in the inner surf, Thornton and Guza (1982) measured $H_{\mathrm{rms}} = 0.42h$. Sallenger and Holman (1985) found $\gamma_{\mathrm{rms}} = H_{\mathrm{rms}}/h$ of 0.29–0.55, increasing with bed slope and independent of deep-water steepness, a range that spans the saturation measurements at Torrey Pines and Duck (Thornton and Guza, 1982; Sallenger and Holman, 1985; Raubenheimer et al., 1996). In terms of the surf-similarity (Iribarren) parameter $\xi_0 = \tan\beta/\sqrt{s_0}$ (Battjes, 1974), with $\tan\beta$ the beach slope, gentle slopes (small ξ_0) produce spilling breakers that saturate near $\gamma \approx 0.4$–0.5, and steep slopes produce plunging or surging breakers at $\gamma \approx 0.8$–1.2.

A value of γ refers to a particular breaking height. The McCowan and Goda limits are the height of a wave at the moment it breaks. The Sallenger–Holman range is a root-mean-square height averaged over the waves in the inner surf. The self-calibrated index is the significant wave height formed from the mean of each wave's three largest face heights at 1 Hz (Sec. 2.2.1). Two values of γ can be compared only when they refer to the same height.

2.2.8. Boundary cells

A boundary cell is the most seaward cell of the breaking zone, the last cell offshore in which waves break. The heights there belong to waves at the moment of breaking, which is what the McCowan and Goda limits describe. The index table places each wave where it is tallest, on that edge or shoreward of it, and the depth table follows the broken wave toward shore. The depth inversion therefore uses a wider band than the breakpoint limits, and those limits are larger than the index the depth table gives.

2.2.9. Analysis windows

Each camera's index and depth field are estimated on the same window, the 14 days before each survey: 20 September to 3 October 2025 in Fall (to 2 October at Oceanside Pier North) and 20 January to 2 February 2026 in January. Fourteen days is the longest January window that every camera's record supports, because the records of Oceanside Pier South and Harbor North Jetty begin on 20 January, and the Fall windows use the same length.

A window must be long enough for the data to fix both the per-cell intercepts and the slope. It needs enough depth-limited cells for the intercepts $\{a_i\}$ and enough tide range to separate the slope from them. Three conditions express this: at least 500 cells hold data, at least 20 of them enter the estimate of γ_{sc}, and the sampled tide spans at least 0.9 m. Of the 15 fourteen-day windows, 14 meet all three. The January window at Oceanside Harbor has 398 cells with data; it is kept, and its results are read with that caveat.

The January field at Tamarack is also inverted with the Fall index, which tests whether an index read once carries over to a later survey period.

2.3. Validation

2.3.1. Per-camera metrics

Recovered depth is compared cell by cell with the survey of the same period, on the cells whose survey depth lies below MLLW. The offset is the mean difference between recovered depth and survey depth, positive where the recovered depth is too deep. It is removed per camera before RMSE is computed, which separates the recovered spatial pattern from its vertical offset. The offset and the RMSE with no offset removed are reported as well. A camera is scored where at least 50 cells (450–1,600 m^2, depending on cell size) overlap the survey. The correlation, r, and the slope of the regression of survey depth on recovered depth are reported only where at least 100 cells (900–3,100 m^2) overlap and the survey depth has a standard deviation $\sigma(d_{\mathrm{GT}})$ of at least 0.2 m. These cameras are called r-valid.

2.3.2. Study-site metrics

The RMSE over the study sites combines every scored camera. The study-site r and slope combine only the r-valid cameras, after each camera's mean is removed from both recovery and survey. RMSE and r depend on the scored cell population, so each is quoted with its cell count.

2.3.3. Fixed-index inversions

A fixed-index inversion uses the same per-cell mean height, $\bar{H}_i$, and mean tide, $\bar{T}_i$, as the self-calibrated inversion (Sec. 2.2.4); only γ is supplied from outside. The comparison separates the depth information in the height tables from the tide-based estimate of the index. For every scored camera and survey period, the 14-day $\bar{H}_i$ and $\bar{T}_i$ are inverted as $\hat{d}_i = \bar{H}_i/\gamma - \bar{T}_i$ on the scored cells. Three fixed values are tested. The McCowan limit 0.78 is the constant most often imposed. The Battjes–Stive value 0.54, at the Tamarack offshore steepness $s_0 \approx 0.003$, needs a wave model for s_0 but no survey, and the same value is used for every camera. The value 0.42 is the midpoint of the Sallenger–Holman range for wave-averaged heights in the inner surf. Each value is applied to the depth table, whatever statistic it was defined for, as an operational inversion would apply it. The McCowan limit describes a wave at the moment it breaks (Sec. 2.2.8), and it is larger than the index the depth table gives.

For each survey the level-matching index γ_m is computed as well: the value that makes the offset zero on the scored cells, $\gamma_m = \sum_i \bar{H}_i / \sum_i (d_{\mathrm{GT},i} + \bar{T}_i)$. It uses the survey and serves only as a reference for γ_{sc}.

2.4. Satellite-derived bathymetry

2.4.1. Retrieval and calibration

SDB follows the published method of Caballero and Stumpf (2020). The retrieval switches between blue/red and blue/green band ratios and combines four scenes. Pixels in optically deep water, too deep for the seabed to affect the reflectance, are masked (Caballero and Stumpf, 2023). Retrievals deeper than the method's depth limit are discarded; the limit is set where the calibration fit stops converging, or from the Secchi depth – the depth at which a white disc lowered from the surface is no longer visible, which indicates how deep the seabed remains optically detectable. Following Babbel et al. (2021) and Ma et al. (2020), the ratio is calibrated on seabed photons from the ICESat-2 ATL24 product (Magruder et al., 2025a,b), whose accuracy Parrish et al. (2025) assess at eight validation sites. No survey depths enter the retrieval. After quality control the calibration used 512 photons in Fall and 440 in January, from ten acquisition dates between 2019 and 2024.

2.4.2. Survey-period composites

One retrieval per survey period covers the whole survey area. It combines the four cleanest Sentinel-2 Level-2A scenes between 30 August and 19 October 2025 for Fall, and between 9 January and 6 February 2026 for January. In Fall the blue/red ratio was usable in shallow water ($|r| = 0.43$ with the calibration depths), and the published switch to blue/green offshore was kept. In January blue/red fell below the method's threshold ($|r| = 0.10$ against 0.25), so blue/green was used throughout.

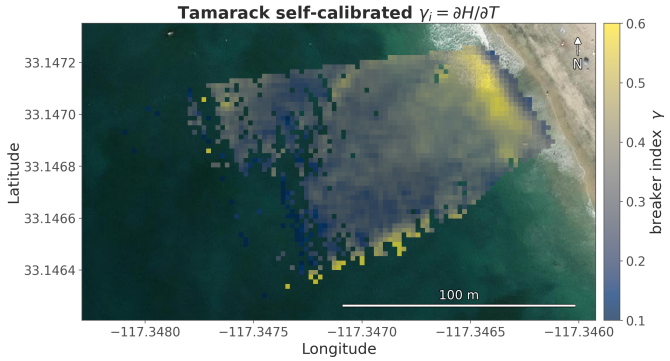


Figure 3: Map of the per-cell tide slope $\gamma_i = \partial H/\partial T$ at Tamarack in the Fall-2025 window (20 September–3 October 2025), fitted separately in each 2 m cell with Eq. (10) from the individual pocket heights and drawn over satellite imagery with a north arrow and a 100 m scale bar true at 33.147°N. The index γ_{sc} itself is read from the index table on 3 m cells (Secs. 2.2.1 and 2.2.5). Cells whose tide bins span less than 0.20 m are left out, because two adjacent tide bins give a two-point slope; slopes outside 0–1.6 are not drawn, and the map is shown with a 3 × 3-cell running mean. The color scale runs from $\gamma_i = 0.1$ (dark blue) to 0.6 (yellow). The band 10–20 m seaward of the landward edge, along the active whitewater line, gives $\gamma_i \approx 0.45$–0.55 (yellow), around $\gamma_{sc} = 0.50$. Seaward of it γ_i falls to 0.30–0.35 and, beyond 60 m, to about 0.25 (blue to gray).

2.4.3. Comparison design

Two further runs bound the comparison. The bare single-scene log-ratio of Stumpf et al. (2003), without masks or compositing, is the historical baseline. The other is the published method calibrated on survey depths outside the scored camera's footprint. SDB and the camera inversion are scored as in Sec. 2.3, each with its own offset removed, on the cells where both exist. The SDB offset is reported, since a retrieval calibrated on ICESat-2 carries its own datum and tide offset. The comparison uses the same camera-grid cells as the study-site validation.

3. Results

3.1. Breaker index at Tamarack

The Fall window runs for 14 days, from 20 September to 3 October 2025. It holds 6.4×10^5 pocket heights from 1,077 clips (180 h of video), sorted into cells and into six tide bins between 0.0 and 1.7 m above MLLW. On the index table $\gamma_{sc} = 0.50$, and the common slope $\hat{\gamma}$ of Eq. (11) on the same table is 0.40.

In the map of γ_i (Fig. 3), the band 10–20 m seaward of the landward edge, along the active whitewater line, gives $\gamma_i \approx 0.45$–0.55, around the self-calibrated index. Seaward of it γ_i falls to 0.30–0.35, and beyond 60 m to about 0.25. The index is read on that band, where the slopes are largest.

3.2. Depth recovery at Tamarack

Equation (12) converts the depth table of each window to depth with that window's index. On the 14-day window ending at the Fall survey, with $\gamma_{sc} = 0.50$, the mean recovered depth is within 0.1 m of the survey (0.06 m shallower), and the RMSE is 0.32 m on 1,098 cells (9,900 m^2, $r = 0.70$; Fig. 4B). On the 14-day window ending at the January survey, with $\gamma_{sc} = 0.59$, the mean recovered depth is again within 0.1 m (0.02 m shallower), and the RMSE is 0.42 m on 1,053 cells (9,500 m^2, $r = 0.68$; Fig. 4G). No offset was removed from these means; the RMSE is the scatter about them. Differences of a few centimetres in these offsets are below the method's systematic uncertainty and are not interpreted. The level-matching index, the value that makes the offset zero, is 0.49 in Fall and 0.58 in January. Because it is computed on the depth table while γ_{sc} comes from the index table, its agreement with γ_{sc} to within 0.01 shows that the index transfers between the two tables (Sec. 2.2.1).

Transfer of the index between survey periods. The index at Tamarack is 0.50 in Fall and 0.59 in January. Inverting the January window with the Fall index instead gives an RMSE of 0.43 m ($r = 0.68$) and places the mean depth 0.23 m too deep.

Depth dependence of the bias. Sorted by survey depth, the January recovery goes from 0.23 m too deep at 0.5–1.0 m to 0.90 m too shallow at 3–4 m (Table 2). The regression of recovered depth on survey depth has slope 0.59. That equals $r = 0.68$ times the ratio of the recovered spread to the survey spread, 0.86. A straight line with that slope reproduces every depth band to within 0.22 m.

3.3. Depth recovery across the study sites

Table 1 lists the recovery for each camera, and Fig. 2B–I shows the January fields. The three Fall cameras cover 6.5 km of coast and the ten January cameras 8.3 km. The eleventh January camera, Artificial Reef 1, overlaps the survey on 49 cells, below the 50 needed for a score. The RMSE over all scored cameras is 0.36 m on 3,546 Fall cells (3.2 ha) and 0.47 m on 4,510 January cells (6.2 ha). Per-camera RMSE ranges from 0.25 to 0.83 m. On the r-valid cameras, $r = 0.90$ on the same 3,546 Fall cells and 0.66 on 3,922 January cells (5.5 ha). The Fall value is dominated by Oceanside Pier South, which holds 2,023 of those cells with $r = 0.96$; the other two Fall cameras give 0.70 and 0.58.

The mean offsets reach 1.04 m at The Rock in January, where the map is 1.04 m too shallow. Tamarack's mean offsets are 0.06 m and 0.02 m (Sec. 3.2). Of the 13 camera fields (3 in Fall and 10 in January), 10 have negative offsets and are too shallow. γ_{sc} ranges from 0.50 to 0.68 across these fields. The larger offsets, near 1 m, are traced to less precise camera georeferencing: some cameras were calibrated with high precision RTK GPS control points, others from less precise phone GPS or visual landmarks. Because calibration requires a site visit, the practice is not yet uniform across the network, and SCI is working to standardize it.

The fields reach shallow water. Of the scored cells, 674 in Fall (19%) and 657 in January (15%) lie less than 1 m below MLLW. In Fall the recovered fields also cover 49 cells up to 0.3 m above MLLW, which the scoring leaves

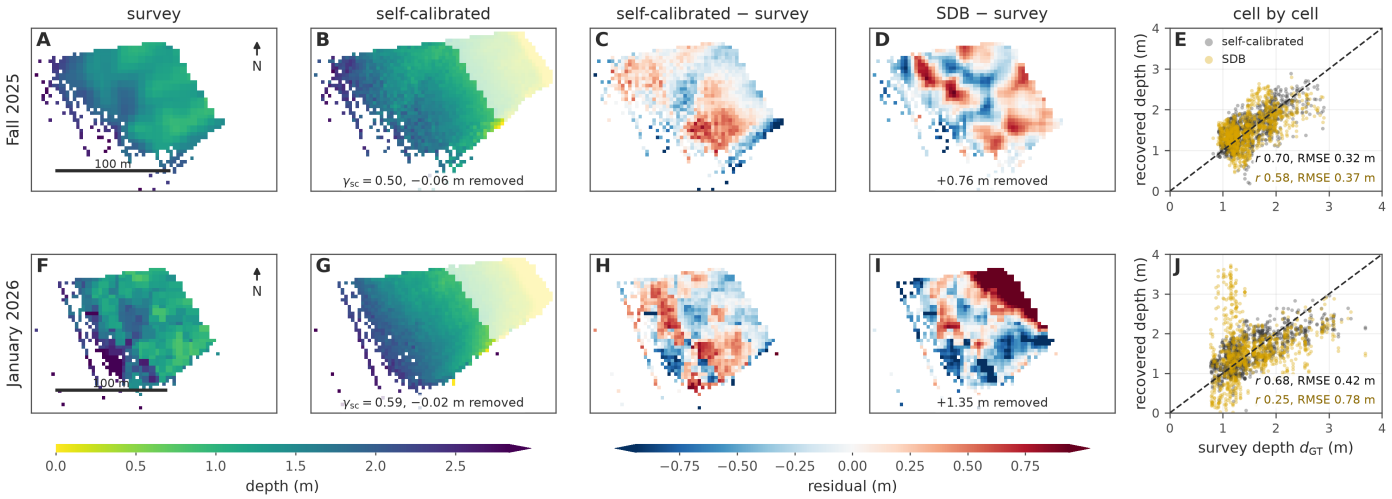


Figure 4: Self-calibrated depth and Sentinel-2 SDB compared with the two surveys at Tamarack, Fall 2025 (A–E, 1,098 cells, 9,900 m^2) and January 2026 (F–J, 1,053 cells, 9,500 m^2), on the cells of Table 1. **(A, F)** Survey depth, with a north arrow and a 100 m scale bar true at 33.147°N. **(B, G)** Self-calibrated depth with the index of each period, $\gamma_{sc} = 0.50$ and 0.59, on the depth scale of A and F; the cells beyond the survey are faded. **(C, H)** Its residual against the survey. **(D, I)** The residual of Sentinel-2 SDB with the published method, calibrated on ICESat-2 and sampled onto the 3 m camera grid, on the same diverging scale. Each field is shown with its constant offset to the survey removed, and the amount removed is printed on B, D, G and I. **(E, J)** Cell-by-cell scatter of both fields against the survey (black: self-calibrated; gold: SDB), with r and the RMSE after offset removal. The figure compares the spatial pattern recovered by the camera inversion and by SDB with the survey in both periods.

Table 1: Depth recovery of the self-calibrated inversion for each camera on the 14-day windows. n is the number of scored cells, $\sigma(d_{GT})$ the survey-depth spread in meters and γ_{sc} the camera's self-calibrated index (Sec. 2.2.5) from its own window. RMSE (m) is computed after removing each camera's offset, the mean recovery–survey difference, which is listed in the last column and is positive where the recovered depth is too deep. The larger offsets come from GPS errors in the camera georeferencing (Sec. 3.3). r and slope are withheld (n/a) where fewer than 100 cells (900–3,100 m^2) overlap or $\sigma(d_{GT}) < 0.2$ m; RMSE and offset are still reported for Artificial Reef 2, Harbor South Jetty and Tyson Street. The "All scored" row gives the RMSE over every scored camera and the "r-valid" row the r and slope over the r-valid cameras. The table shows how well each camera recovers the survey.

Camera	n	$\sigma(d_{GT})$	γ_{sc}	RMSE	r	slope	offset
Fall 2025							
Oceanside Pier South	2023	1.02	0.57	0.29	0.96	1.05	−0.57
Tamarack	1098	0.40	0.50	0.32	0.70	0.68	−0.06
Oceanside Pier North	425	0.81	0.53	0.67	0.58	0.81	−0.67
All scored (RMSE)	3546	n/a	n/a	0.36	n/a	n/a	n/a
r-valid cameras	3546	0.85	n/a	0.36	0.90	1.00	n/a
January 2026							
Tamarack	1053	0.55	0.59	0.42	0.68	0.79	−0.02
Oceanside Pier South	788	0.53	0.57	0.83	0.74	0.34	0.15
North Carlsbad	682	0.31	0.57	0.25	0.64	0.73	0.61
The Rock	618	0.34	0.66	0.30	0.85	0.55	−1.04
Harbor North Jetty	457	0.51	0.68	0.41	0.67	0.66	−0.23
Artificial Reef 2	265	0.06	0.64	0.37	n/a	n/a	−1.02
Harbor South Jetty	255	0.19	0.66	0.28	n/a	n/a	−0.24
Oceanside Harbor	166	0.25	0.58	0.36	0.25	0.19	0.11
Oceanside Pier North	158	0.30	0.64	0.35	0.64	0.42	−0.85
Tyson Street	68	0.12	0.53	0.56	n/a	n/a	−1.01
All scored (RMSE)	4510	n/a	n/a	0.47	n/a	n/a	n/a
r-valid cameras	3922	0.46	n/a	0.49	0.66	0.46	n/a

out. Cells more than 500 m from The Rock are excluded because the position error there exceeds the cell size; this removes 246 January cells that overlap the survey. With them, that camera would score 0.33 m on 864 cells instead of 0.30 m on 618.

3.4. Fixed breaker indices

On the cells of Table 1, after offset removal, the three fixed indices (McCowan 0.78, Battjes–Stive 0.54 and the Sallenger–Holman midpoint 0.42; Sec. 2.3) return RMSEs of 0.36–0.45 m in Fall and 0.39–0.63 m in January over all scored cameras, against 0.36 and 0.47 m for the self-

Table 2: Mean bias $\langle \hat{d} - d_{\mathrm{GT}} \rangle$ of the self-calibrated inversion at Tamarack, by survey-depth band, against the January-2026 survey on the 1,053 cells of Table 1, after the constant offset is removed. Negative values are recoveries shallower than the survey, and "cells" is the number of cells in each band. The table shows that the bias falls steadily with survey depth, from +0.23 m in the shallowest band to −0.90 m at 3–4 m, the pattern of a recovered depth whose regression on survey depth has a slope of about 0.59 (Sec. 3.2).

Depth band (m)	cells	bias (m)
0.5–1.0	119	+0.23
1.0–1.5	502	+0.12
1.5–2.0	234	−0.04
2.0–2.5	113	−0.20
2.5–3.0	65	−0.55
3.0–4.0	20	−0.90

calibrated index. Over the r-valid cameras, r differs by at most 0.02 between the four indices, and the slope of survey depth on recovered depth rises with the index, from 0.75 to 1.36 in Fall and from 0.35 to 0.58 in January. Without offset removal, the RMSE over all scored cameras is 1.21, 0.56 and 0.56 m in Fall and 0.82, 0.70 and 0.99 m in January for the McCowan, Battjes–Stive and Sallenger–Holman values, against 0.61 and 0.74 m for the self-calibrated index. At Tamarack it is 0.98, 0.39 and 0.54 m in Fall and 0.56, 0.43 and 0.72 m in January, against 0.32 and 0.42 m.

The inversions differ in vertical offset. At Tamarack the McCowan limit places the field 0.93 and 0.38 m too shallow, and the Sallenger–Holman midpoint 0.40 and 0.56 m too deep. The Battjes–Stive value places it 0.24 m too shallow in Fall and 0.11 m too deep in January. The self-calibrated index places it 0.06 and 0.02 m too shallow (Sec. 3.2). Over all scored cameras the mean absolute offset is 0.41 and 0.40 m for Battjes–Stive against 0.42 and 0.41 m for the self-calibrated index, and Battjes–Stive has the smaller offset at 6 of the 13 camera fields. Both are more than 1 m too shallow at Tyson Street.

3.5. Satellite-derived bathymetry

Study-site aggregate. Over all cameras, Sentinel-2 has offset-removed RMSEs of 0.88 m in Fall and 0.81 m in January, against 0.36 m and 0.48 m for the camera inversion, on 3,546 Fall and 4,468 January cells. It is less accurate in the shallowest depth band in both periods, and more accurate only at 2–4 m in January. SDB covers all comparison cells except 42 of the 166 Oceanside Harbor cells in January.

Tamarack. At Tamarack in Fall, on 1,098 cells, the offset-removed SDB RMSE is 0.37 m against 0.32 m for the camera inversion, with an offset of +0.76 m against −0.06 m (Fig. 4D, E). At Tamarack in January, on 1,053 cells, the corresponding RMSE is 0.78 m against 0.42 m, with an offset of +1.35 m against −0.02 m (Fig. 4I, J).

Depth dependence. In Fall, the SDB RMSE is 0.94 m in the 0–1 m band, 0.92 m at 2–3 m and 1.45 m at 3–4 m, against 0.36 m and 0.32 m for the camera inversion in the two deeper bands. Before offset removal SDB reads the 0–1 m band 1.07 m too deep and the 3–4 m band 1.46 m too shallow. In January, the SDB RMSE is 1.16 m in the 0–1 m band, which it reads 2.29 m too deep before offset removal. At 2–3 m in January the RMSE is 0.51 m for SDB and 0.55 m for the camera inversion, and at 3–4 m it is 0.71 m and 1.08 m.

Correlation and calibration sensitivity. On the r-valid cameras (3,546 and 3,880 cells) SDB has $r = 0.27$ in Fall and $r = 0.02$ in January, against 0.90 and 0.66. Its offset ranges from −0.03 to +3.10 m between cameras covered by the same composite. The bare single-scene log-ratio gives $r = -0.10$ and -0.14. Calibrated on survey depths outside each scored camera's footprint, the published method has RMSEs of 2.04 m in Fall and 0.99 m in January.

3.6. Swell–tide coupling

A coupling window is a period that contains the 14-day windows of one survey period. Over the Tamarack January coupling window, 28 December 2025 to 10 February 2026, the per-clip tide and the daily-median LOTUS s_0 give $\rho_{Ts_0} = +0.089$. With $\gamma'(\langle s_0 \rangle) \approx 13$ from the Battjes–Stive form, (8) gives a bias of 0.006–0.009 in cells 2–3 m deep ($\langle h_i \rangle$), less than 2% of γ_{sc}. The calculation needs no survey and was run on 46 coupling windows, one per camera and survey period: 21 southern California cameras in Fall and 25 in January. At $\langle h_i \rangle = 2$ m the bias does not exceed 0.019 in any of them. It reaches 0.051 only on microtidal cameras elsewhere in Surfline's network, where the tidal range is three to seven times smaller.

4. Discussion

4.1. Spatial pattern and absolute depth scale

Offset-removed RMSE primarily tests the spatial pattern and cannot by itself identify the breaker index. Within a camera footprint the survey depth has a standard deviation of only 0.06–1.02 m (Table 1). At Tamarack, changing from the self-calibrated index to the McCowan limit changes the offset-removed RMSE by at most 0.01 m while moving the vertical offset by 0.4–0.9 m. Where $r < 1$, the lowest offset-removed RMSE occurs when the recovered spread is r times the survey spread. A larger index flattens the recovered field through $\hat{d} = \bar{H}/\gamma - \bar{T}$, which explains the lower January RMSE of the McCowan inversion.

At Tamarack the self-calibrated index places the mean depth 0.06 and 0.02 m too shallow, while the Battjes–Stive value places it 0.24 m too shallow in Fall and 0.11 m too deep in January. Over the study sites the two have almost the same mean absolute offset, 0.42 and 0.41 m against 0.41 and 0.40 m, but the Battjes–Stive value requires offshore steepness from a wave model.

The January depth-band trend at Tamarack has a regression slope of 0.59 (Sec. 3.2) and may reflect compression of the recovered field or cell-scale errors in the survey. Possible sources of compression are blur in the projected wave

positions, unsaturated cells in the outer depth bands and an index that varies with depth. These effects are not separated here.

The two wide surveys differ by an RMS of 0.21 m on the 18,369 co-located cells shallower than 4 m, with a mean difference of less than 0.1 m; over all 262,735 co-located cells the RMS is 0.14 m. The near-zero mean shows no net gain or loss of sand along the surveyed coast over the winter, but sand moved within it. At Tamarack the two surveys differ by 0.26 m RMS on the 1,053 January-scored cells with a mean difference of less than 0.1 m. The bar and the deeper pocket in the middle of the field shift between panels A and F of Fig. 4. Near Oceanside Pier the mean difference within a camera field reaches 0.5–0.75 m. There the Fall depths come from the interpolated nearshore patches (Sec. 2.1.5) and the January depths from the vessel survey, so the difference includes that between the two products. The 0.21 m is therefore an upper bound on the disagreement of two surveys of the same surf zone, part survey noise and part change, and an offset-removed RMSE near it is as close to a survey as a second survey would be. Local changes of this kind, at the scale of a camera field over a season, are what daily camera maps can follow. At Tamarack, the recoveries of both periods agree better with the Fall survey than with the January survey on the cells both cover. The Fall recovery scores 0.31 m against its own survey and 0.42 m against the January survey, and the January recovery 0.42 and 0.30 m. On these cells the January survey has the larger depth spread, 0.50 and 0.55 m against 0.41 and 0.45 m. Over all cameras that both surveys cover, the Fall recoveries score 0.28 and 0.35 m against the Fall and January surveys, and the January recoveries 0.51 and 0.56 m. Part of the lower January accuracy is therefore tied to cell-scale error in the January survey rather than to the recovery.

An index below the level-matching value places the field too deep; unsaturated waves or a positive constant height error can have the same effect. An index above the level-matching value places the field too shallow, as occurs in 10 of the 13 camera fields. Selecting the largest median among noisy distance bins can bias γ_{sc} high, while a negative height or datum error shifts the field shallow without changing the index. The mean offset reaches 1.04 m at The Rock, so the absolute depth of some single-camera maps remains uncertain by more than a meter. One known depth can remove the vertical offset but cannot distinguish an additive error from an error in the breaker index.

4.2. Measurement range and update cadence

The recovered fields start at about the low-tide line. Of the scored cells, 19% in Fall and 15% in January lie less than 1 m below MLLW, where the water is under a meter deep at low tide. In Fall the fields also reach 0.3 m above MLLW, into the intertidal zone that waterline methods map. The camera maps therefore reach into the band between the waterline and the deeper water that boats survey easily. The celerity inversions of the Introduction report RMSE of 0.38 m at Duck (Holman and Bergsma, 2021) and 0.43 m on streaming webcams (Andriolo et al., 2025), over wider depth ranges. The Tamarack vertical offsets are no larger than 0.06 m, so RMSE without offset removal rounds to the same 0.32 and 0.42 m reported after offset removal. Over the study sites, RMSE without offset removal is 0.61 and 0.74 m, where the per-camera offsets add to the error. This inversion applies where waves break. cBathy practice discards collections in that condition, once the offshore wave height exceeds about 1.2 m (Holman and Bergsma, 2021).

Each map integrates the 14 days before it, but the window can advance one day at a time, so a rolling window gives a new map every day. Consecutive maps share most of their data, so the time resolution is set by the window length and not by the update interval.

4.3. Comparison with satellite-derived bathymetry

The satellite wave-kinematic method maps coastal depths down to about 100 m at sub-kilometer resolution, with an RMSE of 6–9 m globally (Almar et al., 2021). The color method is accurate to a few decimeters in deeper, clear water (Caballero and Stumpf, 2019; Albright and Glennie, 2021) but has large errors in the shallowest water. Pacheco et al. (2015) found their 0–2 m class the worst, with a bias of +0.61 m, which they attribute to sediment stirred up by breaking. Caballero and Stumpf (2020) describe false shoaling in turbid water. Here SDB was less accurate than the camera inversion in the shallowest depth band and over all cameras, and more accurate only at 2–4 m in January (Sec. 3.5). Its per-camera offset cannot be removed without a survey, and calibrating on survey depths outside each footprint made it less accurate in both periods. The two methods therefore cover different parts of the profile: color-based SDB reaches deeper, clear water, and the camera inversion maps the surf zone, where the color signal fails.

4.4. Limitations

Water level and projection errors. The harmonic tide prediction is made for a fixed list of tide stations, not for the beach itself. All eleven cameras use the San Clemente station (Sec. 2.1.3), 30–40 km north of the cameras, and any difference in tidal phase or range between the station and the beach enters the tide record as a time shift and a scale error. The prediction also omits storm surge and wave setup. The effect of these errors on the fitted slope depends on their correlation with the predicted tide, while setup and datum differences also shift the vertical offset. The swell–tide calculation measures coupling between daily values and does not resolve correlations within a tidal cycle caused by daylight sampling or diurnal wind. Any variation in the breaker index or offshore swell that correlates with the tide survives removal of the cell means in (10). The tide-dependent projection also shares the tide's time signature, so a projection error can enter the fitted slope. This effect was not quantified.

Estimator precision and depth scale. The variance of a per-cell slope depends on tide spread and wave count, both of which fall as cells shrink to the ∼3 m scale used here. The wave count at which γ_i becomes stable was not determined. The self-calibrated index ranges from 0.50 to 0.68 across neighboring cameras (Sec. 3.3), more than their breaking regimes plausibly differ, and an index error of that size changes recovered depths by up to a factor of 1.4. The narrow survey overlap cannot fully distinguish such a scale error from spatial compression or sampling effects. A survey spanning several meters of depth across each recovered field is needed.

Coverage and external validation. The inversion applies only where waves break and has no offshore extension. At Tamarack the index was 0.50 in Fall and 0.59 in January, and holding the Fall index moves the January level by 0.23 m; two surveys cannot separate a seasonal change of the index from its scatter between windows. The ATL24 photons used for SDB calibration were acquired in 2019–2024 over a seabed that has since moved. The Fall survey-calibrated SDB run also draws mainly on offshore vessel depths because the survey contains few nearshore points.

5. Conclusions

Surf-zone depth can be recovered from georeferenced wave tracks measured by Surfline cameras. Measured face heights are sorted into fixed cells and tide bins, the breaker index is estimated from how the heights change with the tide, and the depth-limited relation converts the cell means to depth. At Tamarack the inversion recovers two surveys a season apart to 0.32 and 0.42 m RMSE after offset removal, with indices of 0.50 and 0.59 read from the 14 days before each survey. The mean recovered depth is within 0.1 m of both surveys without any correction. The Fall index carried over to January places the level 0.23 m too deep. Consecutive estimates of γ_{sc} would show whether the index is stable between seasons and how often it must be updated, and cameras at point breaks and reefs would show whether it differs between breaker regimes.

Across the study sites the 14-day maps give 0.36 m RMSE after offset removal on three cameras in Fall and 0.47 m on ten in January. The mean offset reaches 1.04 m at The Rock, which limits the absolute accuracy of some single-camera maps due to imprecise camera georeferencing.

The index recovered from the tide response is the breaker index of the wave height used to form it. Here that height is the significant wave height of each wave's top3mean face height, and it gives 0.50–0.59 at Tamarack; the McCowan limit of 0.78 refers to a single wave at the moment it breaks, and the Sallenger–Holman range to the root-mean-square height of the inner surf. A published index can be compared with the self-calibrated one, or substituted for it, only when the two refer to the same wave height.

The recovered fields start at about the low-tide line, and a rolling window gives a new map every day, each integrating the preceding 14 days. Over the camera footprints the inversion is more accurate in the surf zone than Sentinel-2 SDB. The camera method requires several days of breaking waves spanning a usable tidal range. Within that domain, neither a survey nor a wave model is needed to set the breaker index. Run across Surfline's camera network, on cameras already installed and without any equipment deployed or site visited, the method updates the depth band between the low-tide line and the deepest saturated cell, the least current part of most nearshore bathymetry maps. These maps can track sandbar migration, storm recovery and beach nourishment, and give wave, run-up and flood models a current surf-zone bathymetry.

CRediT authorship contribution statement

Ketron Mitchell-Wynne: Conceptualization, Methodology, Software, Formal analysis, Investigation, Writing – original draft. **Michael Reinwald:** Software, Formal analysis, Investigation, Writing – original draft. **Francisco Sansana Silva:** Software, Writing – review & editing. **Daniel Thompson:** Software, Writing – review & editing. **Zane D'Amico:** Software, Writing – review & editing. **Mercedes Stringer:** Software, Writing – review & editing. **Benjamin Freeston:** Supervision.

Declaration of competing interest

All authors are employees of Surfline/Wavetrak, Inc., which operates the camera network described and offers products derived from it commercially. The authors declare no other competing interests.

Data availability

The camera-derived breaking-wave heights and the recovered bathymetry are proprietary to Surfline/Wavetrak, Inc. The RE:BEACH survey data were provided by GHD for the City of Oceanside (GHD, 2026) and are available upon request. The Sentinel-2 Level-2A imagery (Copernicus) and the ICESat-2 ATL24 product (Magruder et al., 2025b) used in Section 2.4 are publicly available.

Declaration of generative AI and AI-assisted technologies in the manuscript preparation process

During the preparation of this work the authors used Claude (Anthropic) to write and refactor analysis and figure-generation code and to edit the text for style and consistency. After using this tool, the authors reviewed and edited the content as needed and take full responsibility for the content of the published article.

Acknowledgements

The authors thank the City of Oceanside, the California Coastal Commission, the RE:BEACH program, GHD and Merkel & Associates for the Oceanside–Carlsbad bathymetric surveys used for validation (GHD, 2026). Funding for the monitoring and data collection that supported the analyses presented in this paper was provided through a grant from the California Coastal Commission to the City of Oceanside.

References

Aarninkhof, S.G.J., Ruessink, B.G., 2004. Video observations and model predictions of depth-induced wave dissipation. IEEE Transactions on Geoscience and Remote Sensing 42, 2612–2622. doi:10.1109/tgrs.2004.835349.

Aarninkhof, S.G.J., Ruessink, B.G., Roelvink, J.A., 2005. Nearshore subtidal bathymetry from time-exposure video images. Journal of Geophysical Research: Oceans 110, 2004JC002791. doi:10.1029/2004jc002791.

Aarninkhof, S.G.J., Turner, I.L., Dronkers, T.D.T., Caljouw, M., Nipius, L., 2003. A video-based technique for mapping intertidal beach bathymetry. Coastal Engineering 49, 275–289. doi:10.1016/s0378-3839(03)00064-4.

Albright, A., Glennie, C., 2021. Nearshore bathymetry from fusion of Sentinel-2 and ICESat-2 observations. IEEE Geoscience and Remote Sensing Letters 18, 900–904. doi:10.1109/LGRS.2020.2987778.

Almar, R., Bergsma, E.W.J., Thoumyre, G., Baba, M.W., Cesbron, G., Daly, C., Garlan, T., Lifermann, A., 2021. Global satellite-based coastal bathymetry from waves. Remote Sensing 13, 4628. doi:10.3390/rs13224628.

Andriolo, U., Azevedo, A., Gonçalves, G., Taborda, R., 2025. Nearshore depth inversion bathymetry from coastal webcam: A novel technique based on wave celerity estimation. Remote Sensing 17, 2274. doi:10.3390/rs17132274.

Arendt, R.G., Fixsen, D.J., Moseley, S.H., 2000. Dithering strategies for efficient self-calibration of imaging arrays. Astrophysical Journal Supplement Series 128, 639–650.

Babbel, B.J., Parrish, C.E., Magruder, L.A., 2021. ICESat-2 elevation retrievals in support of satellite-derived bathymetry for global science applications. Geophysical Research Letters 48, e2020GL090629. doi:10.1029/2020GL090629.

Battjes, J.A., 1974. Surf similarity, in: Proceedings of the 14th International Conference on Coastal Engineering, ASCE, Copenhagen. pp. 466–480. doi:10.1061/9780872621138.029.

Battjes, J.A., Janssen, J.P.F.M., 1978. Energy loss and set-up due to breaking of random waves, in: Proceedings of the 16th International Conference on Coastal Engineering, pp. 569–587.

Battjes, J.A., Stive, M.J.F., 1985. Calibration and verification of a dissipation model for random breaking waves. Journal of Geophysical Research 90, 9159–9167.

Bergsma, E.W.J., Almar, R., 2018. Video-based depth inversion techniques, a method comparison with synthetic cases. Coastal Engineering 138, 199–209. doi:10.1016/j.coastaleng.2018.04.025.

Bergsma, E.W.J., Almar, R., Melo de Almeida, L.P., Sall, M., 2019. On the operational use of uavs for video-derived bathymetry. Coastal Engineering 152, 103527. doi:10.1016/j.coastaleng.2019.103527.

Birrien, F., Castelle, B., Marieu, V., Dubarbier, B., 2013. On a data-model assimilation method to inverse wave-dominated beach bathymetry using heterogeneous video-derived observations. Ocean Engineering 73, 126–138. doi:10.1016/j.oceaneng.2013.08.002.

Brodie, K.L., Palmsten, M.L., Hesser, T.J., Dickhudt, P.J., Raubenheimer, B., Ladner, H., Elgar, S., 2018. Evaluation of video-based linear depth inversion performance and applications using altimeters and hydrographic surveys in a wide range of environmental conditions. Coastal Engineering 136, 147–160. doi:10.1016/j.coastaleng.2018.01.003.

Caballero, I., Stumpf, R.P., 2019. Retrieval of nearshore bathymetry from Sentinel-2A and 2B satellites in South Florida coastal waters. Estuarine, Coastal and Shelf Science 226, 106277. doi:10.1016/j.ecss.2019.106277.

Caballero, I., Stumpf, R.P., 2020. Towards routine mapping of shallow bathymetry in environments with variable turbidity: Contribution of Sentinel-2A/B satellites mission. Remote Sensing 12, 451. doi:10.3390/rs12030451.

Caballero, I., Stumpf, R.P., 2023. Confronting turbidity, the major challenge for satellite-derived coastal bathymetry. Science of the Total Environment 870, 161898. doi:10.1016/j.scitotenv.2023.161898.

Camenen, B., Larson, M., 2007. Predictive formulas for breaker depth index and breaker type. Journal of Coastal Research 23, 1028–1041.

Catalán, P.A., Haller, M.C., 2008. Remote sensing of breaking wave phase speeds with application to non-linear depth inversions. Coastal Engineering 55, 93–111. doi:10.1016/j.coastaleng.2007.09.010.

Cesbron, G., Melet, A., Almar, R., Lifermann, A., Tullot, D., Crosnier, L., 2021. Pan-european satellite-derived coastal bathymetry—review, user needs and future services. Frontiers in Marine Science 8, 740830. doi:10.3389/fmars.2021.740830.

van Dongeren, A., Plant, N., Cohen, A., Roelvink, D., Haller, M.C., Catalán, P., 2008. Beach wizard: Nearshore bathymetry estimation through assimilation of model computations and remote observations. Coastal Engineering 55, 1016–1027. doi:10.1016/j.coastaleng.2008.04.011.

Drusch, M., Del Bello, U., Carlier, S., Colin, O., Fernandez, V., Gascon, F., Hoersch, B., Isola, C., Laberinti, P., Martimort, P., Meygret, A., Spoto, F., Sy, O., Marchese, F., Bargellini, P., 2012. Sentinel-2: ESA's optical high-resolution mission for GMES operational services. Remote Sensing of Environment 120, 25–36. doi:10.1016/j.rse.2011.11.026.

Fixsen, D.J., Moseley, S.H., Arendt, R.G., 2000. Calibrating array detectors. Astrophysical Journal Supplement Series 128, 651–658.

Flater, D., 2026. XTide: Harmonic tide clock and tide predictor. https://flaterco.com/xtide/. Accessed October 2026.

Frugier, S., Almar, R., Bergsma, E.W.J., Bak, S.A., 2026. Standalone color-based bathymetry over 10 years at duck (nc, usa) from optical satellite imagery and wave breaking analysis. Coastal Engineering 203, 104855. doi:10.1016/j.coastaleng.2025.104855.

GHD, 2026. RE:BEACH monitoring survey data, Oceanside, California. Unpublished data prepared for the City of Oceanside; bathymetry collected by Merkel & Associates.

Goda, Y., 1970. A synthesis of breaker indices. Transactions of the Japan Society of Civil Engineers 2, 227–230.

Goda, Y., 2010. Random Seas and Design of Maritime Structures. 3 ed., World Scientific.

Holman, R., Bergsma, E.W.J., 2021. Updates to and performance of the cbathy algorithm for estimating nearshore bathymetry from remote sensing imagery. Remote Sensing 13, 3996. doi:10.3390/rs13193996.

Holman, R., Haller, M.C., 2013. Remote sensing of the nearshore. Annual Review of Marine Science 5, 95–113. doi:10.1146/annurev-marine-121211-172408.

Holman, R.A., Lippmann, T.C., O'Neill, P.V., Hathaway, K., 1991. Video estimation of subaerial beach profiles. Marine Geology 97, 225–231. doi:10.1016/0025-3227(91)90028-3.

Holman, R.A., Plant, N., Holland, T., 2013. cBathy: A robust algorithm for estimating nearshore bathymetry. Journal of Geophysical Research: Oceans 118, 2595–2609. doi:10.1002/jgrc.20199.

Holthuijsen, L.H., 2007. Waves in Oceanic and Coastal Waters. Cambridge University Press.

Lange, A.M.Z., Fiedler, J.W., Merrifield, M.A., Guza, R.T., 2023. Uav video-based estimates of nearshore bathymetry. Coastal Engineering 185, 104375. doi:10.1016/j.coastaleng.2023.104375.

Ma, Y., Xu, N., Liu, Z., Yang, B., Yang, F., Wang, X.H., Li, S., 2020. Satellite-derived bathymetry using the ICESat-2 lidar and

Sentinel-2 imagery datasets. Remote Sensing of Environment 250, 112047. doi:10.1016/j.rse.2020.112047.

Magruder, L., Parrish, C., Perry, J., Holwill, M., Swinski, J.P., Kief, K., 2025a. ICESat-2 coastal and nearshore bathymetry product algorithm development. Earth and Space Science 12, e2025EA004390. doi:10.1029/2025EA004390.

Magruder, L.A., Parrish, C.E., Perry, J., Swinski, J.P., Holwill, M., Kief, K., Corcoran, F., 2025b. ATLAS/ICESat-2 L3A along track coastal and nearshore bathymetry, version 1. NASA National Snow and Ice Data Center Distributed Active Archive Center. doi:10.5067/ATLAS/ATL24.001.

McCowan, J., 1894. On the highest wave of permanent type. Philosophical Magazine, Series 5 38, 351–358.

Miche, R., 1944. Mouvements ondulatoires de la mer en profondeur croissante ou decroissante. Annales des Ponts et Chaussées 114, 25–78, 131–164, 270–292, 369–406.

Pacheco, A., Horta, J., Loureiro, C., Ferreira, O., 2015. Retrieval of nearshore bathymetry from Landsat 8 images: A tool for coastal monitoring in shallow waters. Remote Sensing of Environment 159, 102–116. doi:10.1016/j.rse.2014.12.004.

Parrish, C.E., Magruder, L.A., Perry, J., Holwill, M., Swinski, J.P., Kief, K., 2025. Analysis and accuracy assessment of a new global nearshore ICESat-2 bathymetric data product. Earth and Space Science 12, e2025EA004391. doi:10.1029/2025EA004391.

Plant, N.G., Holman, R.A., 1997. Intertidal beach profile estimation using video images. Marine Geology 140, 1–24. doi:10.1016/s0025-3227(97)00019-4.

Plant, N.G., Holman, R.A., Freilich, M.H., Birkemeier, W.A., 1999. A simple model for interannual sandbar behavior. Journal of Geophysical Research: Oceans 104, 15755–15776. doi:10.1029/1999jc900112.

Raubenheimer, B., Guza, R.T., Elgar, S., 1996. Wave transformation across the inner surf zone. Journal of Geophysical Research 101, 25589–25597.

Reinwald, M., Mitchell-Wynne, K., D'Amico, Z., Stringer, M., Freeston, B., 2026. Breaking-wave height from an operational coastal camera network. Preprint, EarthArXiv; in preparation.

Ruessink, B.G., Pape, L., Turner, I.L., 2009. Daily to interannual cross-shore sandbar migration: Observations from a multiple sandbar system. Continental Shelf Research 29, 1663–1677. doi:10.1016/j.csr.2009.05.011.

Salameh, E., Frappart, F., Almar, R., Baptista, P., Heygster, G., Lubac, B., Raucoules, D., Almeida, L., Bergsma, E., Capo, S., De Michele, M., Idier, D., Li, Z., Marieu, V., Poupardin, A., Silva, P., Turki, I., Laignel, B., 2019. Monitoring beach topography and nearshore bathymetry using spaceborne remote sensing: A review. Remote Sensing 11, 2212. doi:10.3390/rs11192212.

Sallenger, A.H., Holman, R.A., 1985. Wave energy saturation on a natural beach of variable slope. Journal of Geophysical Research 90, 11939–11944.

Salmon, J.E., Holthuijsen, L.H., Zijlema, M., van Vledder, G.P., Pietrzak, J.D., 2015. Scaling depth-induced wave-breaking in two-dimensional spectral wave models. Ocean Modelling 87, 30–47.

Soloy, A., Turki, I., Lecoq, N., Gutiérrez Barceló, Á.D., Costa, S., Laignel, B., Bazin, B., Soufflet, Y., Le Louargant, L., Maquaire, O., 2021. A fully automated method for monitoring the intertidal topography using video monitoring systems. Coastal Engineering 167, 103894. doi:10.1016/j.coastaleng.2021.103894.

Stockdon, H.F., Holman, R.A., 2000. Estimation of wave phase speed and nearshore bathymetry from video imagery. Journal of Geophysical Research: Oceans 105, 22015–22033. doi:10.1029/1999jc000124.

Stumpf, R.P., Holderied, K., Sinclair, M., 2003. Determination of water depth with high-resolution satellite imagery over variable bottom types. Limnology and Oceanography 48, 547–556. doi:10.4319/lo.2003.48.1_part_2.0547.

Surfline, 2020. LOTUS: Surfline's next-generation global swell model. https://www.surfline.com/lp/whatsnew/features/lotus-swell-model. Accessed June 2026.

Thornton, E.B., Guza, R.T., 1982. Energy saturation and phase speeds measured on a natural beach. Journal of Geophysical Research 87, 9499–9508.

Uunk, L., Wijnberg, K.M., Morelissen, R., 2010. Automated mapping of the intertidal beach bathymetry from video images. Coastal Engineering 57, 461–469. doi:10.1016/j.coastaleng.2009.12.002.

Vousdoukas, M.I., Ferreira, P.M., Almeida, L.P., Dodet, G., Psaros, F., Andriolo, U., Taborda, R., Silva, A.N., Ruano, A., Ferreira, Ó.M., 2011. Performance of intertidal topography video monitoring of a meso-tidal reflective beach in south portugal. Ocean Dynamics 61, 1521–1540. doi:10.1007/s10236-011-0440-5.

Weggel, J.R., 1972. Maximum breaker height. Journal of the Waterways, Harbors and Coastal Engineering Division (ASCE) 98, 529–548.

Wilson, G.W., Özkan-Haller, H.T., Holman, R.A., Haller, M.C., Honegger, D.A., Chickadel, C.C., 2014. Surf zone bathymetry and circulation predictions via data assimilation of remote sensing observations. Journal of Geophysical Research: Oceans 119, 1993–2016. doi:10.1002/2013jc009213.

Zhang, C., Li, Y., Cai, Y., Shi, J., Zheng, J., Cai, F., Qi, H., 2021. Parameterization of nearshore wave breaker index. Coastal Engineering 168, 103914.